

Shape and motion of drops sliding down an inclined plane

By NOLWENN LE GRAND, ADRIAN DAERR
AND LAURENT LIMAT

Laboratoire de Physique et Mécanique des Milieux Hétérogènes (PMMH)
UMR 7636 of CNRS, ESPCI, 10 rue Vauquelin, 75231 Paris Cedex 05, France, and
Fédération de Recherche Matières et Systèmes Complexes, UMR 7057 of CNRS, Université de
Paris 7, 4 place Jussieu, 75005 Paris, France

(Received 2 August 2004 and in revised form 28 April 2005)

We report experiments on the shape and motion of millimetre-sized drops sliding down a plane in a situation of partial wetting. When the Bond number based on the component of gravity parallel to the plane Bo_α exceeds a threshold, the drops start moving at a steady velocity which increases linearly with Bo_α . When this velocity is increased by tilting the plate, the drops change their aspect ratio: they become longer and thinner, but maintain a constant, millimetre-scale height. As their aspect ratio changes, a threshold is reached at which the drops are no longer rounded but develop a ‘corner’ at their rear: the contact line breaks into two straight segments meeting at a singular point or at least in a region of high contact line curvature. This structure then evolves such that the velocity normal to the contact line remains equal to the critical value at which the corner appears, i.e. to a maximal speed of dewetting. At even higher velocities new shape changes occur in which the corner changes into a ‘cusp’, and later a tail breaks into smaller drops (pearling transition). Accurate visualizations show four main results. (i) The corner appears when a critical non-zero value of the receding contact angle is reached. (ii) The interface then has a conical structure in the corner regime, the in-plane and out-of-plane angles obeying a simple relationship dictated by a lubrication analysis. (iii) The corner tip has a finite non-zero radius of curvature at the transition to a corner, and its curvature diverges at a finite capillary number, just before the cusp appears. (iv) The cusp transition occurs when the corner opening in-plane half-angle reaches a critical value of about 45° .

1. Introduction

Contact line dynamics are encountered in many everyday situations and especially in industrial coating processes (Kistler & Schweizer 1997), from offset printing to the chocolate-frosting of candy. But the dynamics of wetting, although of interest in a wide range of industrial applications, still lacks a fully satisfactory physical description. Here we focus our interest on a well-defined and apparently simple problem: what happens when a liquid drop slides down a uniform, inclined plane in a situation of partial wetting? At what velocity does it slide and what shape does it assume to accommodate capillary effects and drop motion?

Perhaps unexpectedly, these problems have received rather little attention. Available studies mostly focused on static or quasi-static drops: on yield conditions, i.e. the onset of movement of the drops (Bikerman 1950; Furmidge 1962; Dussan V. & Chow 1983), and on drop velocity just above onset, when the shape of the drops

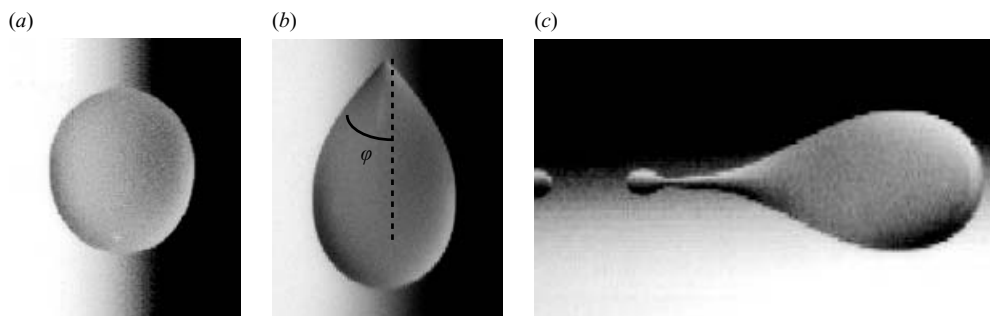


FIGURE 1. Drops sliding down a partially wetting solid surface, pictures from Podgorski (2000). (a) Rounded drop, (b) corner, (c) pearling drop. Motion is from top to bottom in (a) and (b), and from left to right in (c).

remains nearly circular (Dussan V. 1985; Kim, Lee & Kang 2002). However, there is little work on the motion and shape of the drops far above the onset. In a recent experiment, our group performed careful observations on silicone oil drops sliding down a glass plate coated with fluoropolymers (Podgorski, Flesselles & Limat 2001). They showed that unexpected shape changes occur when the velocity U of the drop is increased. When U exceeds a critical value U_c , the drops are no longer rounded as in figure 1(a) and a ‘corner’ develops at their rear (figure 1b). Such singularities are surprising considering the large capillary pressure which the high surface curvature induces near the corner tip. At higher velocities other shape changes occur in which a ‘cusp’ forms and, for even higher velocities, a liquid tail develops at the corner tip, leading to droplet deposition, which is referred to as ‘pearling’ (figure 1c).

These phenomena were qualitatively related to previous observations of what happens when a plate or a tape is pulled out of a bath at the same conditions of partial wetting. Above the critical velocity U_c (maximum speed of dewetting), a triangular film edged by two contact lines forming a similar corner is entrained on the tape with droplet deposition at the corner tip (Blake & Ruschak 1979). In both cases (drops and tapes), this transition to a corner shape is assumed to postpone a forced dynamic wetting transition (Blake & Ruschak 1979; Podgorski *et al.* 2001), in turn assumed to occur when the dynamic receding contact angles vanishes (a hypothesis first proposed by Derjaguin & Levi 1964). To summarize, its inclination allows the contact line to move normally to itself at the critical velocity U_c , while the whole drop (or tape) moves at a larger velocity U . The corner opening angle is thus linked to the drop or plate velocity by a ‘Mach cone type’ relationship of the kind $U_c = U \sin \varphi$. These qualitative considerations leave unresolved the detailed theoretical understanding of these surprising shape changes of sliding drops, that have become a challenge for theoretical modelling. So far, only the rounded to corner transition has been investigated (Ben Amar, Cummings & Pomeau 2001, 2003), and also the interface and flow structure in the corner tip (Stone *et al.* 2001; Limat & Stone 2004). In Ben Amar *et al.* (2001, 2003) a saddle-point structure of the corner tip is assumed, which allows one to both impose a vanishing contact angle at contact line and limit the pressure divergence. On the other hand, in Stone *et al.* as in Limat & Stone (2004), the interface is assumed to take a conical, self-similar, structure, which increases the pressure divergence usually involved in hydrodynamic models of contact line dynamics (Voinov 1976; Cox 1986).

In the present paper we revisit the experiment by Podgorski and co-workers with a new, improved, setup. A simple visualization method enables us to get simultaneous

pictures of the drops taken from above and from the side. These two simultaneous views provide information on the three-dimensional structure of the interface which was impossible with our previous visualization method. An appropriate lighting gives a very strong contrast to these pictures (the drops appearing black on a light background) from which several geometrical quantities are extracted as a function of the capillary number, including the dynamic contact angles and the opening angles of the corner. Among other results, we found that in the corner regime the interface at the rear of the drop has a conical structure, and that this structure appears for a non-zero value of the dynamic receding contact angle. This contrasts with what was commonly believed up to now (Blake & Ruschak 1979; Podgorski *et al.* 2001; Ben Amar *et al.* 2001). Also, the tip of the cone is in fact rounded at small scale, its curvature diverging progressively until the cusp regime appears.

There are several motivations for the present study. Firstly, understanding the corner formation is important for coating applications (Kistler & Schweizer 1997) where this effect limits the efficiency of coating devices (maximal speed of wetting or dewetting, dynamic wetting failure, air trapping, etc.). Secondly, there has recently been great interest in singularity formation at interfaces (Cohen & Nagel 2002), with possible applications for micro-fabrication (encapsulation processes, etc.). When a corner is formed on a sliding drop, there is a point singularity at the intersection of two line singularities (contact lines), which can be important for deposition on a solid surface. Finally, it is one of the simplest wetting experiments that one can imagine to test available contact line models (Voinov 1976; de Gennes 1986; Cox 1986; Blake & Ruschak 1997; Pomeau 2000; Eggers 2005). Here we compare our measurements of dynamic contact angles at the front and rear of the drops to four of these models.

The structure of our paper is as follows. In §2, we first describe the experiment and specify its physical conditions (fluid, surface, image acquisition, etc.). In §3 we describe qualitatively the different regimes observed (oval drops, corner, cusp, and pearling drops). In §4 we present quantitative results concerning the motion of the drops (onset of motion, dependence of the velocity on plate inclination, etc.). In §5 we investigate the evolution of the shape of the drops for increasing capillary number, through several quantities: aspect ratio, dynamic contact angles, and opening angles of the corner. Finally, in §6, we present a synthesis of the results, attempting to give a unified picture of the evolution of drop shapes when the capillary number (i.e. the drop velocity) is changed. We also try to establish connections with recent available models of the corner (Stone *et al.* 2001; Limat & Stone 2004; Ben Amar *et al.* 2001). Preliminary measurements and a brief account of some of the results in this paper are available in two recent European Coating Symposia (Limat *et al.* 2001; Daerr *et al.* 2003).

2. Experimental setup

As depicted in figure 2, millimetre-size drops of silicone oil are emitted at a frequency of about 0.5 Hz by a capillary tube (Pasteur pipette) connected to a syringe pump. The drops fall onto the top of a 22×22 cm glass plate coated with fluoropolymers (FC-725 by 3M) which provide partial wetting conditions for silicone oils (Podgorski 2000), the static contact angles being close to 50° . Using silicone oils (PDMS: $\text{CH}_3[\text{Si}(\text{CH}_3)_2\text{O}]_n\text{Si}(\text{CH}_3)_3$) allows us to vary the viscosity η (via the polymer chain length n) over two orders of magnitude at almost constant surface tension and density. The main characteristics of the oils used are summarized in table 1.

The drops slide down the inclined plate at constant speed – the terminal velocity is reached within a few millimetres from impact – and constant shape. The volume of

Label	Polymerization degree n	Viscosity η (cP)	Density ρ (kg m^{-3})	Surface tension γ (mN m^{-1})
47V10	9	10.0 ± 0.2	936 ± 2	20.1
47V100	75	103.7 ± 0.2	964 ± 2	20.9
47V1000	338	1035 ± 5	970 ± 2	21.1

TABLE 1. Characteristics of the silicone oils used.

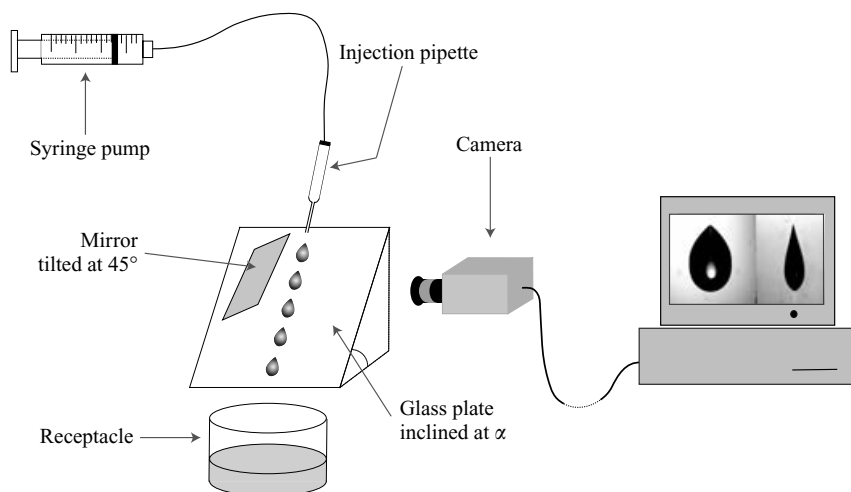


FIGURE 2. Description of the experimental setup.

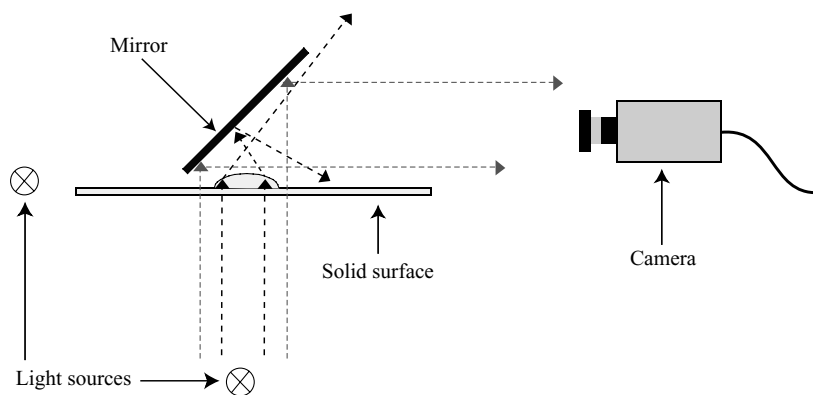


FIGURE 3. In our visualization method, the drops appear dark on a light background. This diagram is in the plane perpendicular to both the inclined plate and the direction of drop motion.

the drops is fixed ($V = (6.0 \pm 0.2) \text{ mm}^3$), and we use the plate inclination as a control parameter to change the drop velocity.

The drop motion and shape are recorded from the side by a video camera whose optical axis is perpendicular to the trajectory of the drops, and at a very small angle with the inclined glass plate. A mirror is suspended above the drop at 45° tilt with respect to the glass plate, so that the camera simultaneously records the direct lateral view and the top view seen in the mirror (figure 3). This visualization method

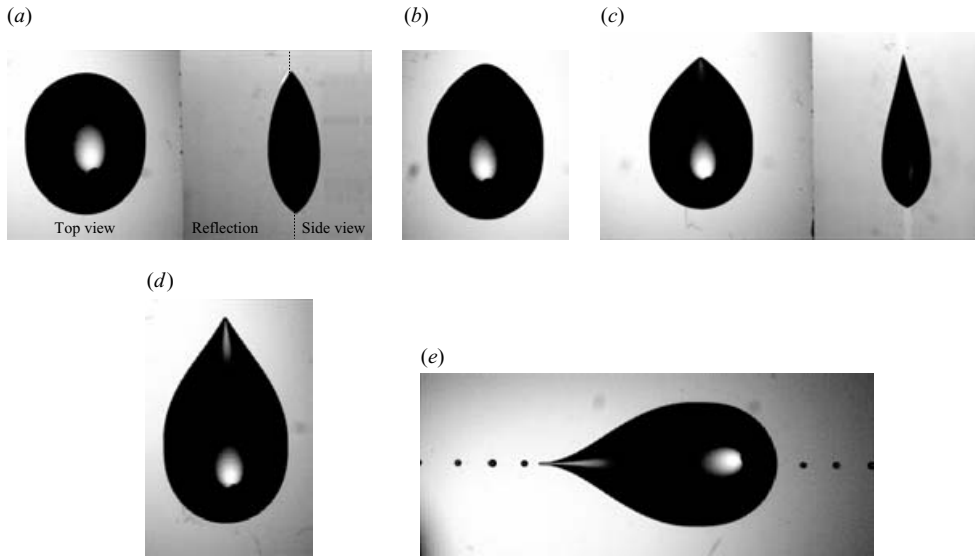


FIGURE 4. Top views (along with side views for (a) and (c)) of drops sliding down an inclined plate for increasing velocities, $\eta = 104$ cP. (a) Oval drop $Ca = 2.85 \times 10^{-3}$, (b) corner $Ca = 4.95 \times 10^{-3}$, (c) corner $Ca = 5.14 \times 10^{-3}$, (d) cusp $Ca = 7.07 \times 10^{-3}$, (e) pearls $Ca = 7.19 \times 10^{-3}$. The motion is from top to bottom except for (e) where it is from left to right.

gives information on the three-dimensional structure of the interface which was not achieved with previous visualizations. We made use of a 'FAST CAM' high-speed video camera, not so much because of its high acquisition frequency as for the high quality of the images produced and the small size of its CCD (1/4 in.) which simplified the optical tunings (step-up ring of 10 mm and a 12.5–75 mm zoom lens). In order to maximize the image contrast (silicone oil being transparent), two light sources are placed at a great distance behind and below the drops (see figure 3).

The light sources are extended enough to produce a white background across the imaged area, but localized enough so that the almost parallel light rays going through a drop are deviated away from the diaphragm by the oblique liquid–air interface. As a result the drops appear black on a white background, except for the centre of the top view where a small image of the light source can be seen. Figures 4(a) and 4(c) give examples of the simultaneous top and side views of the drops (respectively on the left- and right-hand side of the picture). The side view shows the reflection of the drop in the glass plate in addition to the drop itself. From the movies we extract the velocity of the drops for different plate inclinations, as well as geometrical quantities including the advancing and receding dynamic contact angles, as will be detailed in § 5.2.

3. Description of the different drop regimes

At different steady speeds (obtained by changing the plate inclination), the drops adopt different shapes which are particularly easily discriminated by looking at the top views. At low velocities the drops take an oval shape as shown in figure 4(a). If the velocity of the drops is increased, a corner develops at their rear. This transition seems at first continuous: the radius of curvature of the contact line at the rear decreases, and two straight line segments appear on both sides of the tip. Consequently, there is first a 'rounded-corner' (figure 4b), and only for higher velocities does the tip appear

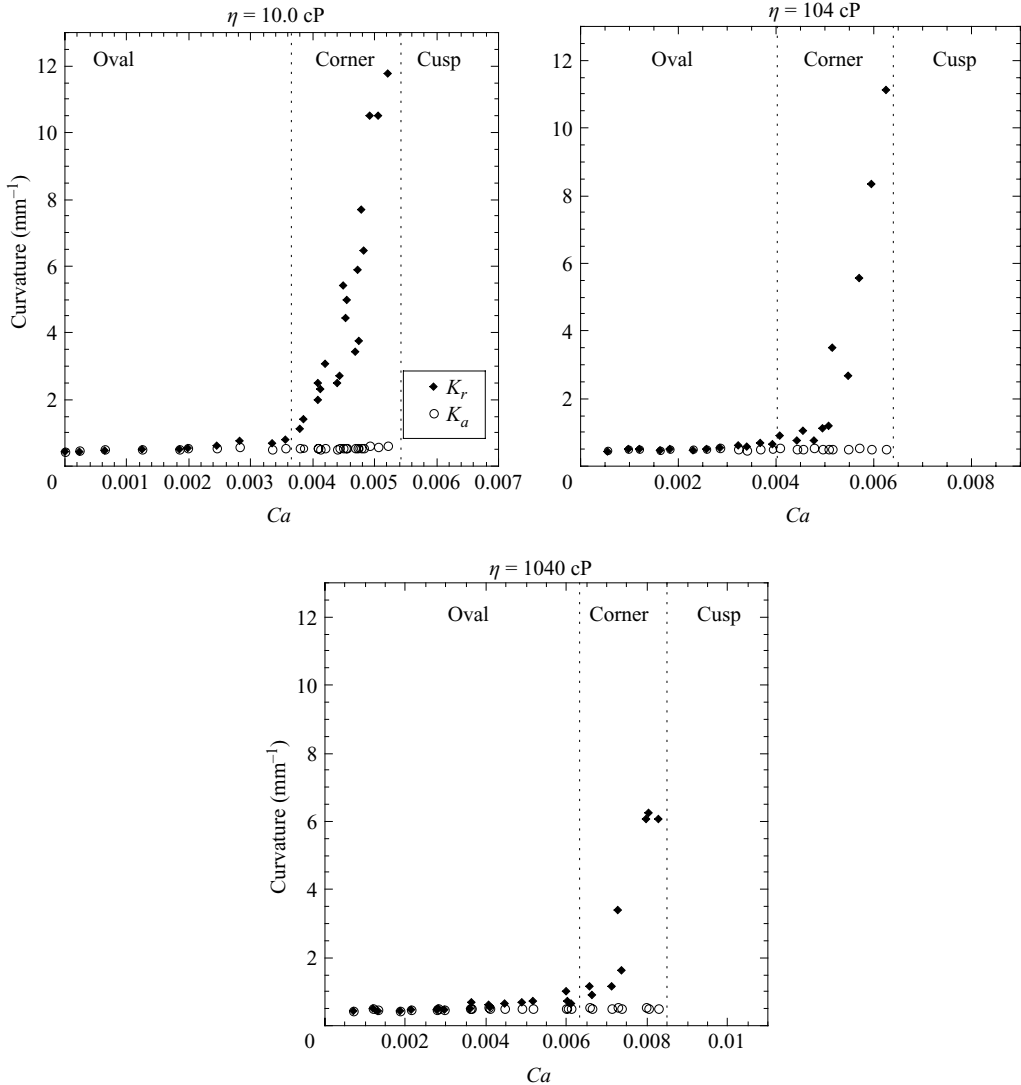


FIGURE 5. In-plane curvatures at the front K_a and rear K_r of the drops seen from above as a function of Ca . The oval-to-corner transition is defined by the sudden variation of the angle φ that decreases from 90° , following a $1/Ca$ law (see figure 14). This also corresponds to the point at which K_r rises above K_a .

to be sharp (figure 4c). We will see that the distinction between the oval and the corner regime is justified by the corner in-plane opening angle which defines a precise transition point (§ 5.4.1): it varies sharply from 90° to smaller values just at this transition. The corner shape is surprising, considering that surface tension is usually thought to oppose the formation of such a singularity. As one can judge from the side views, the interface has a conical structure when the corner regime is well enough developed. This point will be discussed in more detail in § 5.4.4.

To describe the ‘oval’ to ‘corner’ transition more accurately, the curvatures in the plane of the substrate, measured at the front K_a and at the rear of the drops K_r , are plotted in figure 5 versus the capillary number $Ca = \eta U/\gamma$ (defined through

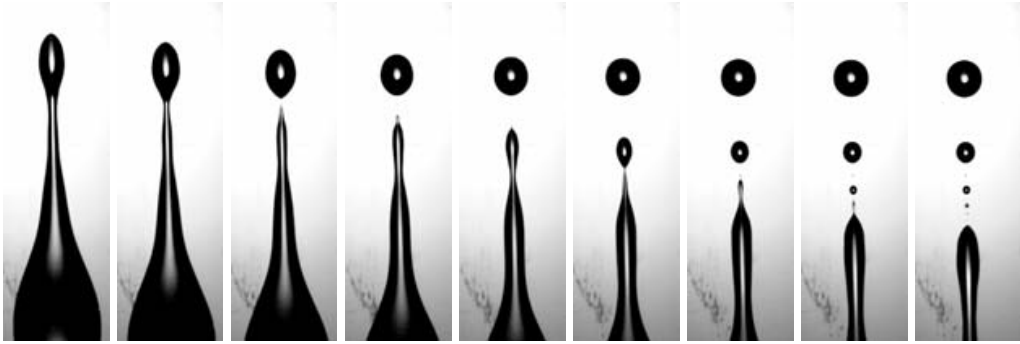


FIGURE 6. Pinching-off in the pearling regime and cascade of smaller drops deposited, $\eta = 104 \text{ cP}$, $Ca = 15 \times 10^{-3}$, $1/3 \text{ s}$ between two pictures.

the drop velocity U , the liquid viscosity η and its surface tension γ), along with a description of the observed shapes. The curvature at the front of the drop remains practically constant, whatever the regime. On the contrary, the curvature at its rear is equal to the front curvature only for a stationary or slowly moving drop, and it increases rapidly at higher velocity. It can be noted that the point at which K_r rises above K_a corresponds to the transition from oval drops to corners. We can see that the curvature at the rear remains finite throughout the corner regime, but sharply diverges for a finite capillary number, which seems to coincide with the transition from ‘corner’ to ‘cusp’. Indeed, for even higher velocities, a cusp begins to form at the rear of the drop, i.e. the contact line is bent outwards close to the tip (figure 4*d*). It is remarkable to see that this shape change occurs precisely at the capillary number at which the curvature of the tip diverges.

Above yet another critical velocity, a pearling transition characterized by the emission of droplets from the tip of the cusp occurs (figure 4*e*). The size of the droplets increases with the velocity of the drops, and eventually the pinching-off produces a cascade of smaller droplets in a process akin to the pinching-off below a dripping faucet (see figure 6).

4. Motion of drops

4.1. Velocity of drops and plate inclination

After the drops start sliding down the plate, their steady velocity U is an increasing function of the plate inclination angle α . To illustrate this, figure 7 shows the evolution of the capillary number $Ca = \eta U / \gamma$ versus an effective Bond number based on the component of gravity parallel to the plane: $Bo_\alpha = Bo \sin \alpha = V^{2/3} (\rho g / \gamma) \sin \alpha$, where Bo is the ‘true’ Bond number. These two dimensionless parameters are those used in Podgorski *et al.* 2001. Three forces are acting on the drops: their weight, a viscous drag on the glass plate, and the interfacial forces. The in-plane components of these forces respectively scale as: $\rho V g \sin \alpha$, $-\eta U V^{1/3}$, and $-\gamma V^{1/3} \Delta_\theta$, where the non-dimensional factor Δ_θ depends on the contact angle distribution along the perimeter and on the perimeter shape. The force balance implies the following scaling law:

$$Ca \simeq Bo_\alpha - Bo_c \quad (4.1)$$

where Bo_c is a constant depending on the wetting hysteresis through Δ_θ . This linear scaling of the non-dimensional velocity Ca with plane inclination, $\sin \alpha$, is confirmed

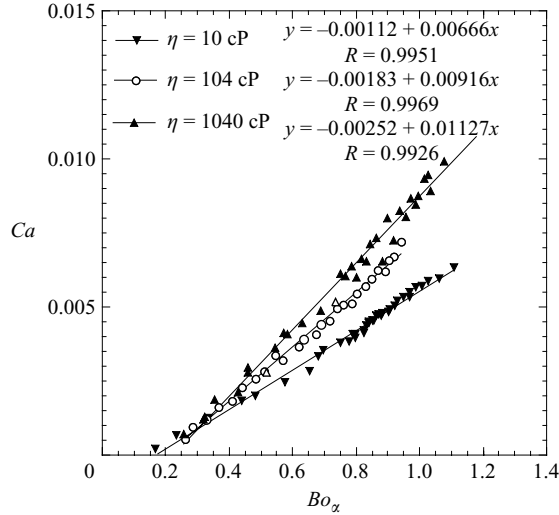


FIGURE 7. Non-dimensional velocity of the drops as a function of plate inclination α . $Ca = \eta U/\gamma$ is the capillary number based on the drop velocity U and $Bo_\alpha = Bo \sin \alpha$ where Bo is the Bond number. R is the correlation coefficient.

Liquid	$\theta_{s,a}$ (deg.)	$\theta_{s,r}$ (deg.)	Hysteresis (deg.)	Theoretical Bo_c	Experimental Bo_c
10.0 cP	50.5 ± 0.5	45.5 ± 0.5	5.0 ± 1.0	0.14 ± 0.03	0.17 ± 0.04
104 cP	52.9 ± 0.5	42.7 ± 0.5	10.2 ± 1.0	0.28 ± 0.03	0.20 ± 0.05
1040 cP	58.1 ± 0.5	46.8 ± 0.5	11.3 ± 1.0	0.32 ± 0.03	0.22 ± 0.05

TABLE 2. Onset of drop motion for three silicone oils on fluoropolymers.

well by the experimental data plotted in figure 7. Note that the data-sets do not completely collapse when represented in non-dimensional units ($Ca = \eta U/\gamma$ as a function of $Bo_\alpha = V^{2/3} \rho g \sin \alpha/\gamma$), small variations in the wetting properties (table 2) being sufficient to explain the different slopes.

4.2. Onset of motion

Drops are at rest at low plate inclinations and start sliding down the plate only above a critical slope, due to contact angle hysteresis. We have experimentally determined the critical slopes for the onset of motion. The corresponding critical Bond number is related to the static contact angle hysteresis $\theta_{s,a} - \theta_{s,r}$ through the shape of the drop (Dussan V. 1985):

$$Bo_c = \left(\frac{24}{\pi}\right)^{1/3} \frac{(\cos \theta_{s,r} - \cos \theta_{s,a})(1 + \cos \theta_{s,a})^{1/2}}{(2 + \cos \theta_{s,a})^{1/3}(1 - \cos \theta_{s,a})^{1/6}} \quad (4.2)$$

where $\theta_{s,a}$ and $\theta_{s,r}$ respectively denote the static advancing and receding contact angles. This equation for Bo_c is only valid for small values of the hysteresis, 10° being a maximum value for $\theta_{s,r} - \theta_{s,a}$. The side views of the drops were used to determine $\theta_{s,a}$ and $\theta_{s,r}$ in the limit of zero velocity (see § 5.2). The hysteresis in our experiments is not always smaller than 10° , but the theoretical values of Bo_c are found to be in rough agreement with the experimental ones (see table 2), the latter varying slightly less with hysteresis than equation (4.2).

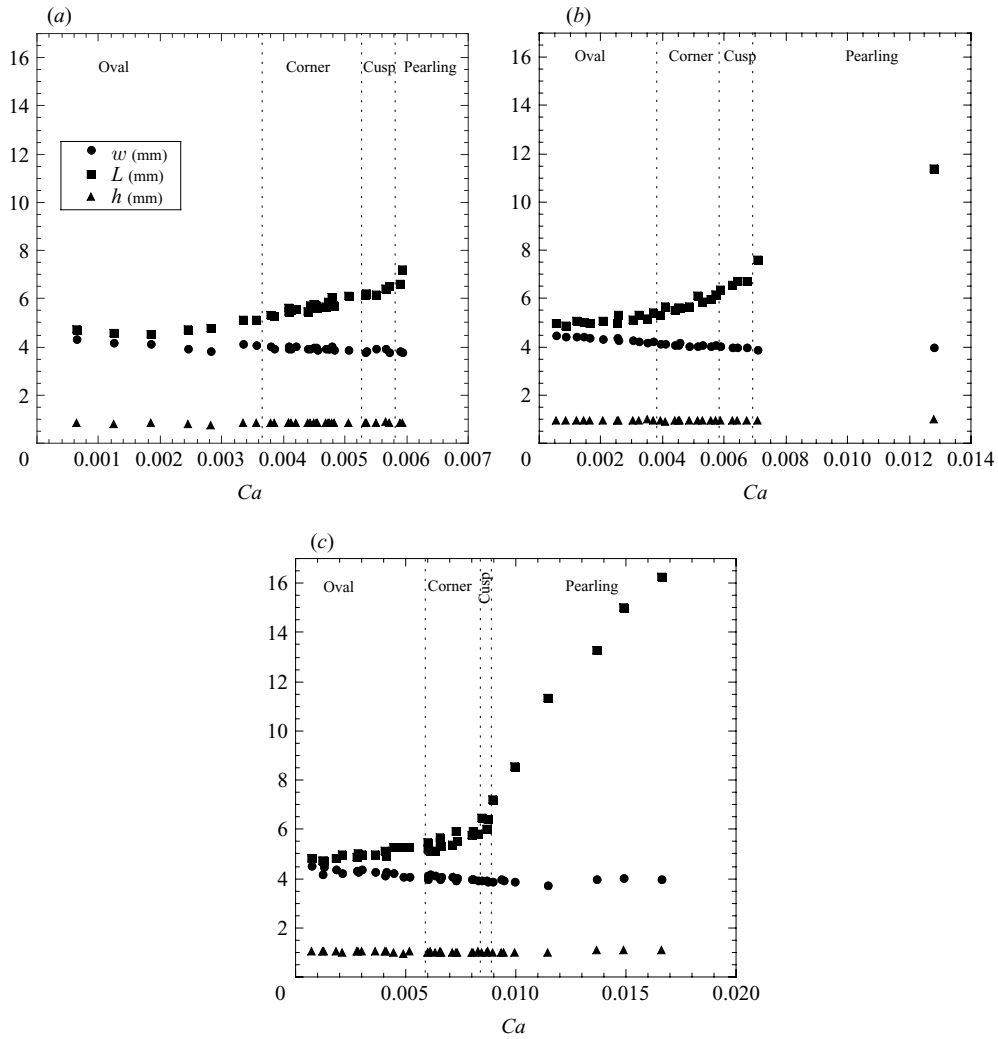


FIGURE 8. Evolution of the length L , width w and height h of drops for (a) $\eta = 10.0$ cP, (b) 104 cP, and (c) 1040 cP.

5. Geometry of the drops

5.1. Aspect ratio of the drops for the different regimes

The length L , width w and maximum height h of the drops have been systematically measured for many inclinations, and are plotted in figure 8. Their evolution for increasing capillary numbers is similar for the three viscosities tested. The most significant variation concerns the length of the drops, which drastically increases in the pearling regime (where L then denotes the maximum length before breakup). The width slowly decreases for increasing capillary numbers, whereas the maximum height remains constant, close to 1 mm, for all three liquids. Thus, as the capillary number increases, the drops get longer and thinner, but keep the same height.

5.2. Dynamic contact angles for rounded drops

Using the side view of a drop, the dynamic advancing contact angle θ_a at the front and the dynamic receding contact angle θ_r at the rear of the drops can be measured.

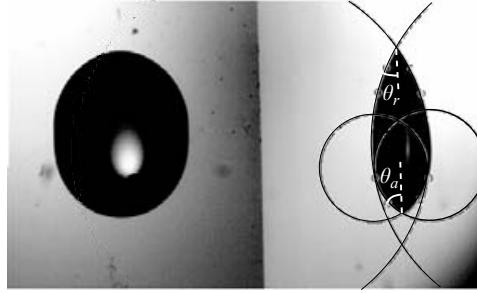


FIGURE 9. Measuring contact angles with circles. The motion is from top to bottom.

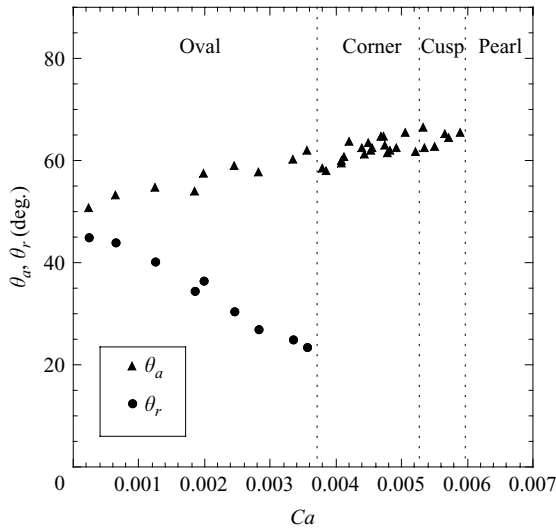


FIGURE 10. Advancing and receding contact angles for $\eta = 10.0$ cP.

This experiment is one of the simplest giving the opportunity to test dynamic wetting models. Figure 9 shows how we measure the contact angles by adjusting two circles tangent to the surface near the tips to fit the contour of the drops. The angle at the intersection of the circles is then calculated. It turns out that interactively adjusting the circles to fit the contour yields a much better precision and reproducibility (typically 1° – 2°) than simply adjusting a wedge made up of two straight line segments. This method gives a macroscopic estimate of the dynamic contact angles at a millimetre scale.

The resulting measurements for silicone oils are plotted as a function of capillary number in figure 10, for $\eta = 10.0$ cP, the plots for the two other viscosities being very similar (see figure 18 below). As expected, the advancing contact angle increases with drop speed, while the receding angle becomes smaller. At rest the angles can range anywhere between the critical values $\theta_{s,a} = 46^\circ$ and $\theta_{s,r} = 51^\circ$. This relatively small interval of 5° , referred to as wetting hysteresis, is another indicator of a very clean and homogeneous surface, in addition to the observed perfectly regular motion of the drop.

The most important observation from the contact angle measurements is that the corner occurs for a finite receding contact angle of about 21° for this viscosity. For a viscosity of 104 or 1040 cP, the critical receding angles for the corner regime

are respectively around 23° and 26° . This contrasts with the hypothesis of Blake & Ruschak (1979) and Podgorski (2000) that the corner shape occurs when the receding contact angle reaches zero.

5.3. Dynamic contact angles: comparison with models

We now compare different models of wetting dynamics to our above experimental data: de Gennes' model, Cox–Voinov's law, a molecular-kinetic model, and finally a linear model of the mobility law linking dynamic contact angles to the capillary number. We start with de Gennes' wetting model (de Gennes 1986) which assumes that the air–liquid interface is locally planar. The liquid therefore forms a wedge, advancing or receding on a solid surface. By writing down an energy balance, truncated at a microscopic dimension a and a macroscopic one b , he obtains

$$\theta(\theta^2 - \theta_s^2) = \pm 6 \ln(b/a)Ca \quad (5.1)$$

where θ_s denotes a statical equilibrium value of the contact angle (hysteresis being neglected). The + symbol refers to an advancing contact line and the – symbol to a receding one. Note that this equation suggests a dynamic forced wetting transition of first order (with discontinuity of contact angle) occurring for $\theta = \theta_s/\sqrt{3}$, whereas all the following models are more consistent with a second-order one. Cox and Voinov's approach (Cox 1986; Voinov 1976) consists in solving Stokes' equations assuming a slowly changing slope of the air–liquid interface, down to microscopic scales. Similar to the approach of de Gennes, the solution is truncated at molecular and macroscopic dimensions, giving the following law:

$$\theta^3 - \theta_s^3 = \pm 9 \ln(b/a)Ca = \pm Ca/A \quad (5.2)$$

where $A = 1/[9 \ln(b/a)]$. The exact formula given by Voinov is more complex, but it can be simplified to that written above for contact angles smaller than $3\pi/4$ (Blake & Ruschak 1997), which is always the case in our experiments here. In the molecular-kinetic model of wetting (Blake & Ruschak 1997; Ruijters, Blake & De Coninck 1999), the approach is very distinct from the two former ones. The dissipation at the contact line is assumed to be dominated by individual molecular displacements at a frequency f , disturbing the adsorption equilibrium at the wetting line. Hence one obtains

$$\theta^2 - \theta_s^2 = \pm \left(\frac{vNkT}{2\pi f L_m \hbar} \right) Ca \quad (5.3)$$

where v is called the molecular flow volume, N the number of adsorption sites per unit area, k the Boltzmann constant, T the absolute temperature, L_m the length of an individual displacement, and finally, \hbar , the reduced Planck constant. It is interesting to note that all the three so-called 'mobility laws' recalled above can be written as $P(\theta, \theta_s) \simeq Ca$ where P is third- or second-order polynomial. This polynomial can of course be linearized at low Ca values, which sometimes enables simplification of calculations of wetting or dewetting flows (Ben Amar *et al.* 2001, 2003; Pomeau 2002). This results in a simplified linear model:

$$\theta - \theta_s \propto \pm U \quad (5.4)$$

that was proposed long ago by Dussan V. (1979), before becoming somewhat forgotten in view of the noticeable curvature of most available experimental data (Blake & Ruschak 1997).

All these possible descriptions of contact line dynamics neglect wetting hysteresis, which complicates the comparison between models and experimental data. A simplification very often encountered, made by most experimentalists, consists in identifying

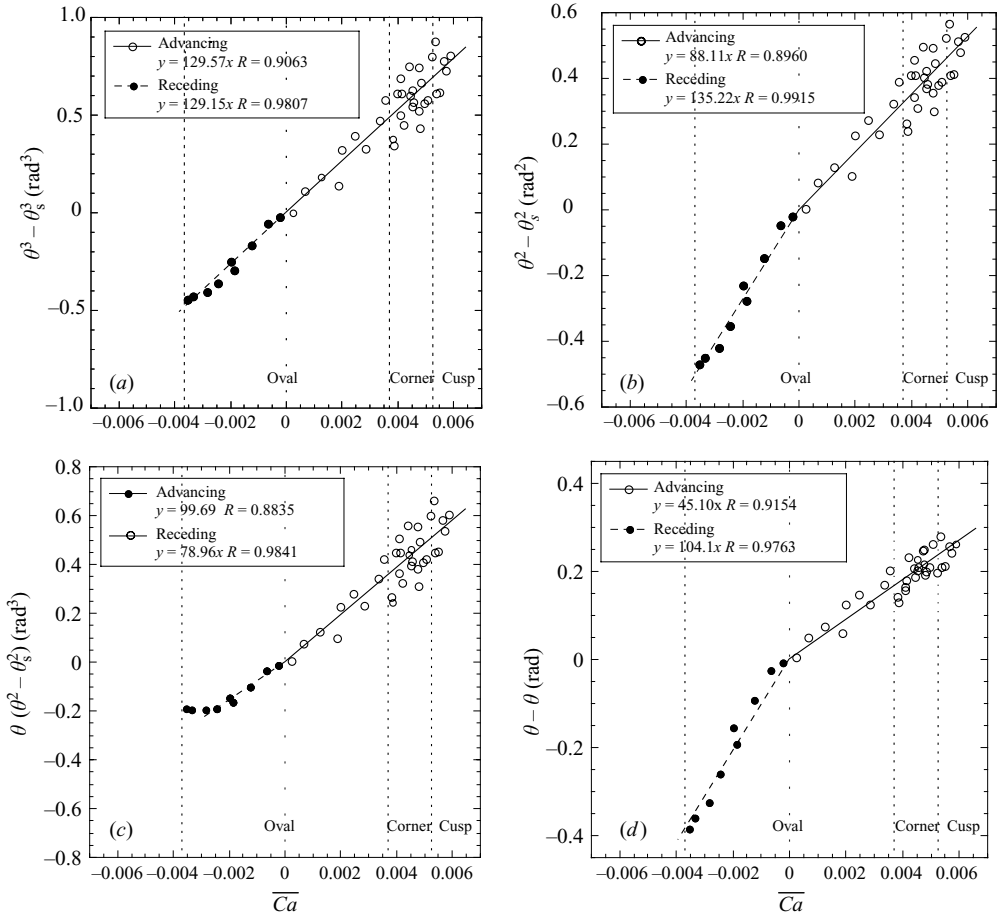


FIGURE 11. Comparison several models for the dynamics of wetting, $\eta = 10.0$ cP. (a) Cox–Voinov, (b) molecular-kinetic, (c) de Gennes, (d) linear. In this figure exclusively, in order to highlight the similarity or discrepancy between the slopes of the advancing and receding parts, the ordinates have been plotted versus the algebraic capillary number \overline{Ca} . \overline{Ca} is positive for the advancing branch and negative for the receding one.

the static contact angle with the limit static angle observed on each branch of the mobility law (i.e. with $\theta_{s,a}$ for the ‘advancing’ curve, and $\theta_{s,r}$ for the ‘receding’ case). This hypothesis has never been proved, but, intuitively, could be reasonable in situations of low hysteresis, as occurs here. Put differently, this point of view implicitly assumes that the hysteresis effect can be reduced to a simple shift of the mobility laws. To simplify the visualization, we found it convenient to plot the quantities $\theta - \theta_s$, $\theta^2 - \theta_s^2$, $\theta(\theta^2 - \theta_s^2)$, and $\theta^3 - \theta_s^3$, versus the algebraic capillary number \overline{Ca} , $\overline{Ca} > 0$ corresponding to the advancing contact line at the drop front, and $\overline{Ca} < 0$ to the receding contact line, and where θ_s has been identified with the static limit angles.

One can see in figure 11 that all these models seem to match the data fairly well in a large range of capillary number. Clearly, our data cannot be used to rule out any of them definitely. On the other hand, each of them is affected by specific drawbacks and has specific advantages. First, de Gennes’ model seems to fail very near the forced wetting transition, where an unexpected ‘plateau’ is observed. Also, the molecular-kinetic model and the linear description do not preserve the symmetry between wetting

Liquid	$a(n)$ (nm)	$a(\sqrt{n})$ (nm)	A for $a = a(n)$	A for $a = a(\sqrt{n})$	Experimental advancing A	Experimental receding A
10.0 cP	3	0.9	8.7×10^{-3}	8.0×10^{-3}	8×10^{-3}	8×10^{-3}
104 cP	20	3	10×10^{-3}	8.7×10^{-3}	9×10^{-3}	12×10^{-3}
1040 cP	100	6	12×10^{-3}	9.2×10^{-3}	13×10^{-3}	13×10^{-3}

TABLE 3. Checking the slopes in Cox–Voinov’s model.

and dewetting: the right- and left-hand parts do not exhibit the same slope at zero capillary number. There is of course no known reason for ‘nature’ to favour this symmetry, but the Cox–Voinov representation of the data does preserve this symmetry. One can check on figure 11(a) that the slope at zero capillary number is indeed the same for both positive and negative capillary number. In this respect, though – again – we cannot extract from our data a definite proof in favour of Cox’s and Voinov’s model, this symmetry is a strong indication in favour of this classical hydrodynamic approach, at least for our experiments on smooth and weakly hysteretic substrates. It is why, in the subsequent sections of our paper we have made use of this model.

Moreover, this symmetry survives a change in viscosity, as can be checked on table 3 for three different oils. For the three oils, the value of the constant $A = 1/[9 \ln(b/a)]$ ($\theta^3 - \theta_s^3 = \pm Ca/A$) is found to be identical, or at least rather close, for both wetting and dewetting. Also, in the same table, it is possible to check that the measured values for A are consistent with orders of magnitude of the relevant spatial scales acting at microscopic scales. The value of the constant $A = 1/[9 \ln(b/a)]$ can be estimated as follows. The typical size of the drops (i.e. 1 mm) will be taken for the macroscopic dimension b , and the size of the molecules of silicone oil (PDMS: $\text{CH}_3[\text{Si}(\text{CH}_3)_2\text{O}]_n\text{Si}(\text{CH}_3)_3$) for the molecular dimension a . Knowing that the distance between a silicon and an oxygen atom in PDMS is $l_{\text{Si-O}} = 0.160$ nm and that the angle $\beta = \widehat{\text{SiOSi}}$ equals 144.0° , gives $l_{\text{Si-Si}} = 2l_{\text{Si-O}} \sin(\beta/2) = 0.30$ nm, and the total length of an accordion-like silicone oil molecule would be $a(n) = nl_{\text{Si-Si}}$. If the molecules are very flexible, the typical diameter of the molecule will be $a(\sqrt{n}) = \sqrt{n}l_{\text{Si-Si}}$, assuming a random walk. We might expect the true molecule size, and microscopic cut-off a , to be somewhere between these two estimates of the molecular dimension. From table 3 we see that the experimental values are in excellent agreement with the corresponding values for A . To our knowledge, this is the first time that a variation in the molecule size is shown to consistently modify the microscopic cut-off length in a hydrodynamic model, and this observation is another indication in favour of this hydrodynamical approach.

Yet, we must also mention that even the Cox–Voinov model has a drawback. As stated above, rather than predicting a forced wetting transition for a non-zero value of contact angle, their model predicts transition for a vanishing contact angle. This is in apparent contradiction with our finding of a non-zero critical value for the appearance of the corner. Only de Gennes’ model predicts such a transition for a non-zero critical angle θ_c . At this point, despite the problems of de Gennes’ model in the description of our data, it is interesting to see if this critical angle we found experimentally is close to that predicted by de Gennes’ approach. In table 4, we report the static angles with the involved hysteresis, the critical angle and the ratio of its value to the receding contact angle for the three oils used. As this table shows, the ratio $\theta_c/\theta_{s,r}$ is close to de Gennes’ prediction $1/\sqrt{3} = 0.577$, at least for the two most viscous oils, but remains definitely smaller. In conclusion, no model seems to describe perfectly

Liquid	$\theta_{s,a}$ (deg.)	$\theta_{s,r}$ (deg.)	Hysteresis (deg.)	Critical θ_c (deg.)	Ratio $\theta_c/\theta_{s,r}$
10.0 cP	50.5 ± 0.5	45.5 ± 0.5	5.0 ± 1.0	21 ± 0.5	0.460 ± 0.015
104 cP	52.9 ± 0.5	42.7 ± 0.5	10.2 ± 1.0	23 ± 0.05	0.540 ± 0.015
1040 cP	58.1 ± 0.5	46.8 ± 0.5	11.3 ± 1.0	26 ± 0.05	0.555 ± 0.015

TABLE 4. Ratio $\theta_c/\theta_{s,r}$ observed experimentally. De Gennes' model would imply a ratio equal to $1/\sqrt{3} = 0.577$.

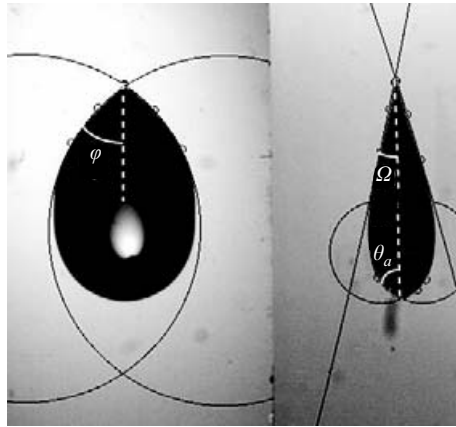


FIGURE 12. Measuring in-plane and out-of-plane opening angles of drops in the corner regime.

and completely our data. The better consistency seems to be reached with the Cox–Voinov model: in this representation, the data preserve the symmetry between wetting and dewetting, but do not exhibit a forced wetting transition at vanishing dynamic contact angle. On the other hand, de Gennes' model recovers the non-zero observed critical angle, but its value is slightly too high and there are problems with the description of the data very near this transition.

5.4. Beyond rounded drops: corners and cusps

We now consider what happens after the transition to a corner shape, and so examine the evolution of the opening angles of the cone from the top views, denoted φ , and from the side views, denoted Ω (figure 12).

5.4.1. In-plane corner opening angle

The in-plane opening angle φ is defined unambiguously for corners, for which we used the ‘circles’ method previously explained in § 5.2, as shown in figure 12. This angle is however more difficult to define for cusped drops since, contrary to the corner drops, there is a sign change in the curvature of the contact line at the rear. As suggested in figure 13, two different estimates of φ have been measured, one defined at the tip of the drops, and the other defined at the change in sign of the contact line curvature, that we call ‘inflection point measurement’. This latter definition corresponds to the angle spanned by the tangents to the contact line at the curvature inflection points, without taking into account the tip of the drop. We found that the ‘inflection point’ definition was more consistent with measurements performed in the corner regime, as shown on figure 14, where we have plotted the evolution of $\sin \varphi$ versus Ca . This

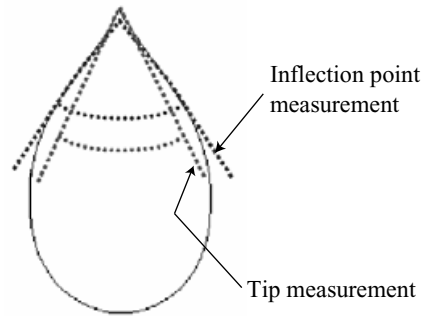


FIGURE 13. Two possible definitions of the angle φ for a cusped drop: ‘inflection point measurement’ and measurement performed at the tip.

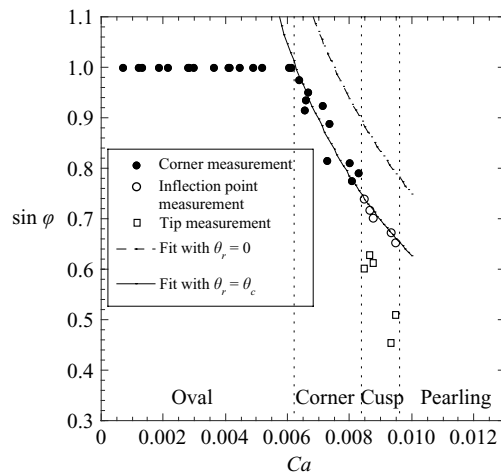


FIGURE 14. Evolution of $\sin \varphi$ versus the capillary number for a viscosity $\eta = 1040$ cP. Dashed line: predictions of equation (5.5), the prefactor being deduced from contact angle measurements on oval drops. Continuous line: predictions of equation (5.6), the critical angle θ_c being the receding contact angle at which the corner is formed.

specific measurement of $\sin \varphi$ for the cusped drops aligns with the corner ones on a continuous curve, suggesting the relevance of the ‘inflection point’ measurement.

As shown on the same figure, $\sin \varphi$ can be fitted with a $1/Ca$ law, as had already been reported by Podgorski *et al.* (2001). In that paper, following ideas going back to Blake and Ruschak (Blake & Ruschak 1979), this $1/Ca$ law and the corner formation itself are explained as follows. When the velocity is progressively increased from zero, the dynamic receding contact angle $\theta_r = f(Ca)$ decreases and vanishes for a critical velocity U_c . At this threshold, a forced wetting transition should occur at which the drop should leave a continuous Landau–Levich film behind itself. To minimize surface energy variations the system would ‘choose’ to incline the contact line with respect to the direction of motion in order to keep the component of velocity normal to the line equal to U_c . If one assumes that the dynamic contact angle is only a function of this normal component of velocity, this statement is equivalent to saying that the ‘corner’ appears when the dynamic contact angle reaches zero and that once it has appeared,

this contact angle stays equal to zero on each of the two tilted contact line segments. Equation (5.2) then implies that

$$\sin \varphi = \frac{\theta_s^3}{9 \ln(b/a)Ca} \propto \frac{1}{Ca}. \quad (5.5)$$

As mentioned above, our contact angle measurements show that the dynamic receding contact angle does not vanish when the corner regime begins, which seems to rule out this interpretation. This is also the case when one tries to directly test equation (5.5) on our data, using the values of $A = 1/[9 \ln(b/a)]$ extracted up above from our contact angle measurements. When plotted on figure 14 (as dashed lines), the law clearly overestimates the measurements of $\sin \varphi$. However, the qualitative argument used by Podgorski and Blake can be valid if one assumes now that in the corner regime the receding contact angle, instead of vanishing, remains always equal to the critical contact angle θ_c identified above, at which the corner appears. This leads to a new law describing $\sin \varphi$, still satisfying a $1/Ca$ dependence, but with a different prefactor:

$$\sin \varphi = \frac{\theta_s^3 - \theta_c^3}{9 \ln(b/a)Ca}. \quad (5.6)$$

As can be seen in figure 14 (continuous line), this law fits the data very well. In summary, we have shown that instead of satisfying a zero contact angle, the corner seems to accommodate a uniform and constant dynamic receding contact angle on each of its two contact lines, this contact angle being equal to θ_c . This is reminiscent of the fact that the forced wetting transition occurs for a non-zero receding contact angle as suggested in de Gennes' model, which value is very close to the θ_c value found in our experiments (see table 4). Let us repeat here that a paradoxical result of our measurements is that the contact angle measurements are better described by a Cox–Voinov model, but the existence of a critical angle is reminiscent of de Gennes' approach. This point remains to be understood.

5.4.2. Contact line velocity

A striking way to point out the oval-to-corner transition consists in plotting the velocity normal to the contact line ($U \sin \varphi$) versus the drop velocity U , or in non-dimensional units, the effective capillary number $Ca \sin \varphi$, defined through the normal velocity, versus the capillary number (figure 15).

It is plain that for oval drops, at the rear, both velocities are equal, and the points align on the the first quadrant bisector. In the corner regime, the curve saturates. This plot highlights that once the capillary number becomes higher than its critical value at which the corner appears, the normal velocity remains constant. The corner transition can thus be viewed as an attempt by the drop to keep its normal speed constant, equal to the critical speed at which the transition occurs. This is of course just another way to interpret equation (5.6): $Ca \sin \varphi = \text{const}$ being equivalent to $\sin \varphi \propto 1/Ca$. This point is obviously connected to the fact explained above that the corner also maintains a constant contact angle equal to θ_c on each of the two contact lines. In fact, it is as if each contact line behaved as a single contact line moving normally to itself, the sole relevant dissipation being associated with the fluid motion in the normal direction. In addition, each contact line is locked to a fixed point characterized by the normal velocity $U \sin \varphi$ and the associated dewetting contact angle, which is in turn governed by the normal component of velocity alone. A more careful analysis of this decoupling between normal and transverse fluid motion is developed in a companion paper (Rio *et al.* 2005).

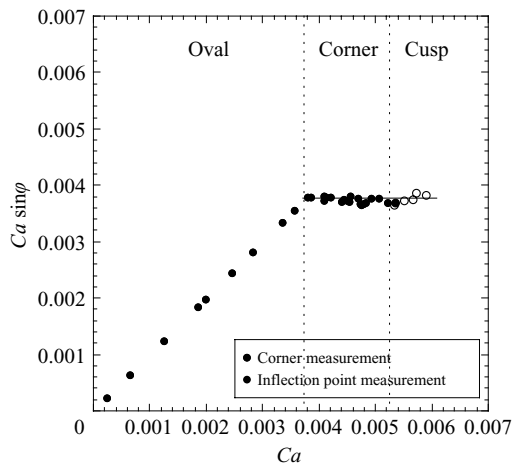


FIGURE 15. Non-dimensional normal speed of contact line at the drop rear versus drop speed (in terms of parameters $Ca \sin \varphi$ and Ca) for $\eta = 10.0$ cP.

We emphasize that the corner transition from oval to corner shape is very well-defined in figure 15, or equivalently that the in-plane corner opening half-angle tends to $\pi/2$ continuously. This means that despite the fact that the apex of the ‘corner’ has a curvature which increases continuously, we recover after the event a clear transition point for the appearance of the corner.

5.4.3. Corner-to-cusp transition

As can be seen on figure 14 for a 1040 cP oil, the transition from a corner to a cusp occurs for an in-plane corner opening half-angle of order 45° . This result is in fact more general and holds for the two other viscosities used (see for instance figure 18, later in the text). Careful analysis of our data leads to a transition angle equal to

$$\varphi = 47^\circ \pm 2^\circ. \quad (5.7)$$

This is somewhat surprising compared to previous results reported by Podgorski (2000), who suggested a transition close to 30° . In fact, Podgorski’s visualization method did not allow very accurate distinguishing of what happened very close to the tip of the drops, and this transition was also instead defined for the pearling regime, both sources of discrepancy being difficult to evaluate. Note however that our value of φ at the transition to a cusp is very close to that in Ben Amar *et al.* (2001), though the model used in that paper (saddle point corner tip) is in contradiction with the conical shape of the interface that we found. This issue clearly deserves more accurate future studies.

5.4.4. Out-of-plane cone angle

Since the tail of the drop has a conical shape (at least when the corner tip becomes highly curved) it is clear that in this regime the angle measured from the side views at the rear of the drop can no longer be interpreted as a receding contact angle. Indeed, the contact line has a singularity at the rear and the vertical cross-section seen on the side views is nowhere perpendicular to the contact line. Instead, a ‘cone opening angle’ is measured, which we denote Ω (see figure 12). We can note however that there is no discontinuity between the values of the receding contact angle θ_r below the critical capillary number of the corner transition and Ω above it, as shown in

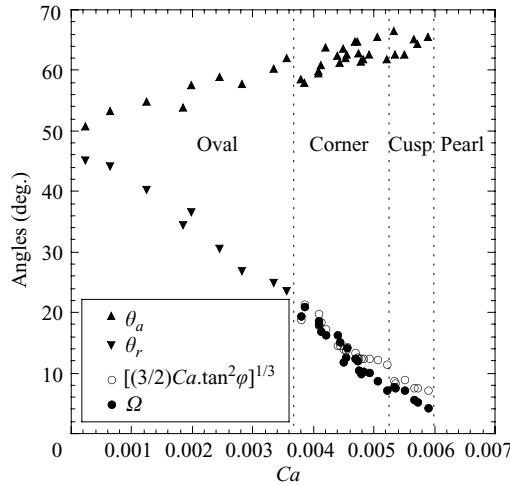


FIGURE 16. Continuity of Ω and θ_r , and comparison between the experimental values of Ω and the Limat–Stone model for a viscosity $\eta = 10.0$ cP.

figure 16. It is also worth noting that above the transition, the values of Ω decrease but are still non-zero at the onset of the pearling regime.

Recently, Limat & Stone (2004) proposed a similarity solution of Stokes’ equation at the rear of a sliding drop, in which the interface has indeed a conical shape. Considering the flow inside the corner in the context of lubrication theory, the authors explain how Ω and ϕ should be related by the following equation:

$$\tan^3 \Omega = \frac{3}{2} Ca \tan^2 \phi. \tag{5.8}$$

A simple approach based on a parabolic estimate and lubrication analysis, as explained in the Appendix, also gives this equation. The plot in figure 16 shows that the measurements of Ω and $[(3/2)Ca \tan^2 \phi]^{1/3}$ match relatively well, which confirms that this model is suitable for the description of the tip of the drops after the corner transition. Since both equation (5.6), giving $\sin \phi = f(Ca)$, and equation (5.8), giving Ω as a function of ϕ , appear to be in good agreement with our data, let us combine them in order to extract a law giving Ω versus Ca :

$$\tan^3 \Omega = \frac{3}{2} Ca \tan^2 \left(\arcsin \frac{\theta_s^3 - \theta_c^3}{9 \ln(b/a) Ca} \right). \tag{5.9}$$

We have compared this law in figure 17 with our data of Ω for the three viscosities used. The agreement is remarkable if one considers the complexity of the physics underlying both equations (5.6) and (5.8), which clearly constitute rather crude estimates of reality. Note however that this representation of the data allows us to show noticeable discrepancies between the experiment and the model. The data obtained in the cusp regime are clearly below the theoretical curve and the expected divergence of Ω near the corner appearance is screened by something that remains unexplained, possibly the fact that the corner is rounded.

6. Conclusion: towards a unified description of corners and related transitions

Concerning the problem of the drop shape, the present study allows us to draw the following conclusions. These are summarized in figure 18, where the angles measured

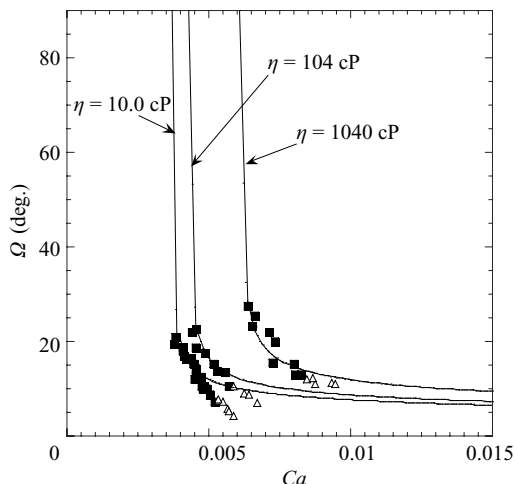


FIGURE 17. Law giving $\Omega = f(Ca)$. The solid lines represent equation (5.9) for all three viscosities. The filled rectangular symbols are for the corners, and the open triangular ones for the cusps.

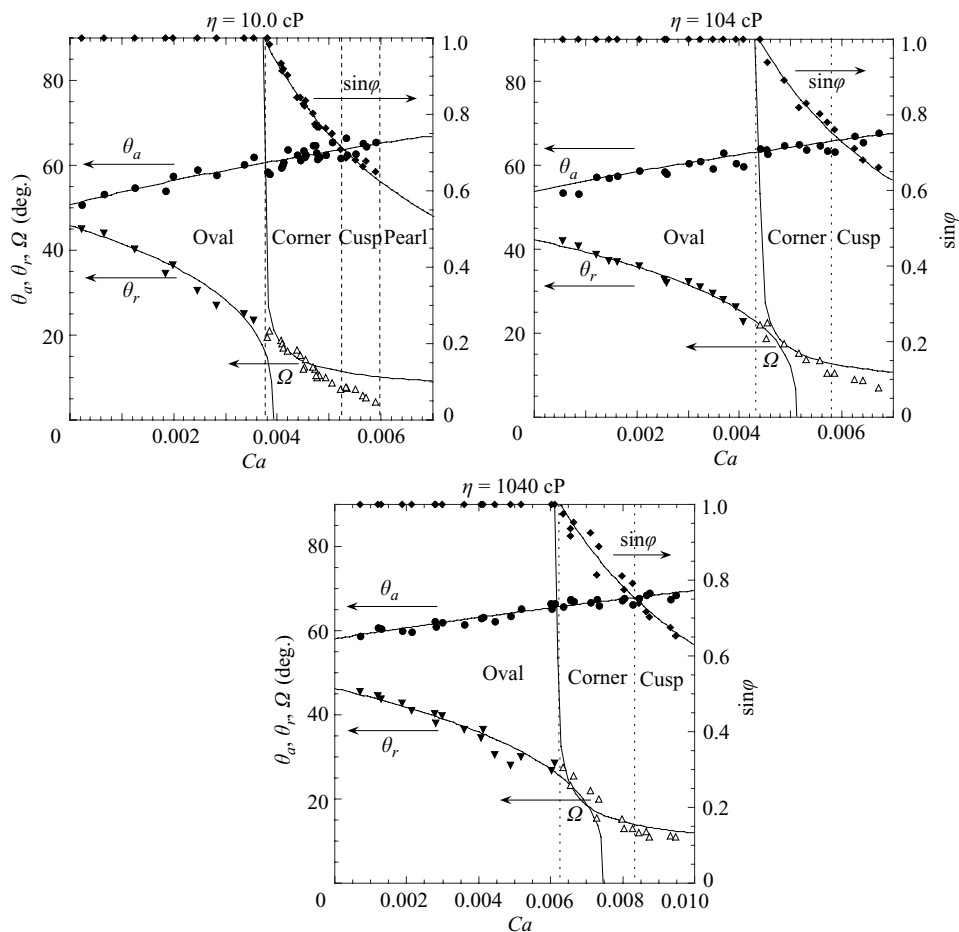


FIGURE 18. Synthesis of results. The solid lines represent the Cox–Voinov law, along with equations (5.6) and (5.9).

are shown in one graph for each viscosity tested, and compared with some of the laws found in the paper.

First, when one considers the dynamic contact angles measured at the advancing and receding front of oval drops, it seems that, when compared to de Gennes' model (de Gennes 1986), to the molecular-kinetic model (Blake & Ruschak 1997), or to a linear model, Cox–Voinov's hydrodynamic model (equation (5.2)) has the best consistency with our measurements. In figure 18, the related fit is superimposed on the data (solid line), and as one can judge from this figure, there is a very good agreement between the model and the data. Let us point out however that the molecular-kinetic and linear models can still be accommodated within the scatter of our data, but the Cox–Voinov model is able to capture the full set of data with the same value of the logarithmic prefactor for both the receding and advancing angle. Though this is not strictly a proof of the validity of this model, this fact is a strong indication in favour of this approach.

It must be recalled that all these wetting models are only valid for the ideal case in which there is no hysteresis at all ($\theta_{s,r} = \theta_{s,a} = \theta_s$). In order to take the hysteresis into account, we have, in a way, subtracted it from the dynamic contact angles, and obtained symmetrical straight lines for Cox–Voinov's model (see figure 11), just as expected without any hysteresis. This seems to show that it is as if the hysteresis simply induced a shift in the curves governing the mobility laws, which is not obvious, as it could also have induced deformations of the curves. However, it must be mentioned that the hysteresis in our experiments is fairly small, and it is possibly the reason why we have avoided complications.

A second important result is that, contrary to what was up to now commonly believed, the transition to a corner occurs for a non-zero value of the receding angle reached at the rear of the drop. This again shows up quite well in figure 18: for the three graphs, the dynamic receding angle is still non-zero when the sine of the in-plane corner opening half-angle φ begins to differ from 1, precisely at the place where the qualitative observations of the drop shape suggest the occurrence of the oval-to-corner transition. It is at present not clear whether the transition to an angular shape in a moving drop is related in some way to a forced wetting transition, as imagined by Podgorski *et al.* (2001), but if one trusts this rather natural idea, our data indicate that such a forced wetting transition should occur for a non-zero value of the dynamic receding contact angle (first-order transition). Surprisingly, this is a property that only de Gennes' model and its recent extensions (de Gennes, Hua & Levinson 1990) are at present able to reproduce. However, this model predicting a transition for a finite contact angle is controversial since the interfacial shape is only treated approximately, neglecting the surface curvature (see Eggers 2004). A puzzling result of our investigations is that the Cox–Voinov model reproduces appropriately the shape of our $\theta(Ca)$ laws, but is unable to explain a first-order forced wetting transition. On the other hand, de Gennes' model does predict a first-order transition, but the predicted shape of $\theta(Ca)$ is clearly inconsistent with the data, at least for the receding branch. A possible explanation of this paradox is perhaps contained in Golestanian & Raphael (2001, 2003). They showed that surface heterogeneities, which are presumably related to contact angle hysteresis, are able to increase the critical angle at which the forced wetting transition occurs. One can thus imagine that a Cox–Voinov approach could coexist with a first-order transition because of this effect. In another direction, one can question the idea of identifying the observed shape transitions with those predicted by mobility laws. The existence of a given shape (rounded, corner, etc.) is a global problem involving both equilibrium equations of the free surface and boundary

conditions at the contact line (see Dussan V. 1985; Ben Amar *et al.* 2003). Perhaps considering the whole global problem instead of the local contact line problem could shift the transition, too.

A third result that we have obtained is that, once the corner is formed (and sufficiently developed), the interface based on the two contact lines involved has a conical structure. This is in agreement with Stone's model of the corner (Stone *et al.* 2001; Limat & Stone 2004) but not with that by Ben Amar *et al.* (2001) who postulate a saddle-point structure of the interface. This is presumably linked to the previous point, i.e. the fact that the contact angle does not reach zero at the corner formation, which allows the formation of a cone. Note however that, except perhaps at the corner-to-cusp transition, the cone is never completely developed, its tip remaining rounded. This suggests considering Stone's model with caution, the completely developed conical structure imagined in these papers being only an idealization of the true structure. Now, although the corner is in fact rounded, the corner formation remains a well-defined transition if one looks carefully at the curves linking the sine of φ to the capillary number. After this transition, just as in Podgorski *et al.* (2001), $\sin \varphi$ follows a $1/Ca$ law, but, as we have shown, the prediction of the prefactor suggests giving up the initial idea of a vanishing contact angle on each of the two contact lines forming the corner. Instead of this, our data are consistent with a dynamic receding contact angle remaining always equal to the critical angle reached at the corner formation. This yields a law of the kind $\sin \varphi = (\theta_s^3 - \theta_c^3)/[9 \ln(b/a)Ca]$, suggested again by the solid lines in figure 18.

Our visualization techniques also allowed us to get information concerning a second angle ruling the conical structure of the interface, i.e. the cone angle Ω viewed from the side. At first sight, the measurements are in continuity with the dynamic receding contact angle θ_r , measured on oval drops. More quantitatively, the data are also consistent with an estimate deduced from the Limat–Stone model (equation (5.8)). Its combination with the law ruling the φ selection (the equation recalled above) leads to a theoretical curve (solid line on the figure 18) that seems to describe reasonably well the data. A puzzling observation is however that this theoretical estimate should diverge at the oval-drop-to-corner transition, which somewhat contradicts the qualitative continuity mentioned above between θ_r and Ω . We believe that this new paradox has its solution in the rounded nature of the corner tip that remains to be taken into account in the model.

Finally, on the three graphs displayed in figure 18, it appears that the transition to cusped drops occurs for $\varphi \sim 45^\circ$, which corresponds to a value predicted by Ben Amar *et al.* (2001). It is therefore possible that the latter model becomes more relevant at high capillary numbers, around the cusp regime where the concave tip geometry could better corresponds to the saddle-point geometry of the model. It must also be emphasized that the curvature eventually tends towards infinity for a finite capillary number, close to this transition to cusps. This could suggest a possible way to deposit a microscopic line on a surface (see Cohen & Nagel 2002).

Many of our results, especially the fact that the tip curvature of the corner is always finite and progressively diverges at the cusp appearance, have been recently recovered by direct numerical simulations involving a disjoining pressure at the contact line (R. V. Roy, private communication). Also, even though Podgorski has already noticed that, as long as one speaks in terms of Bond number, changing the size of the drops does not change their speed and shape (Podgorski *et al.* 2001), it would probably be interesting to investigate the shape and motion of puddles (bigger drops flattened by gravity) sliding down a plane.

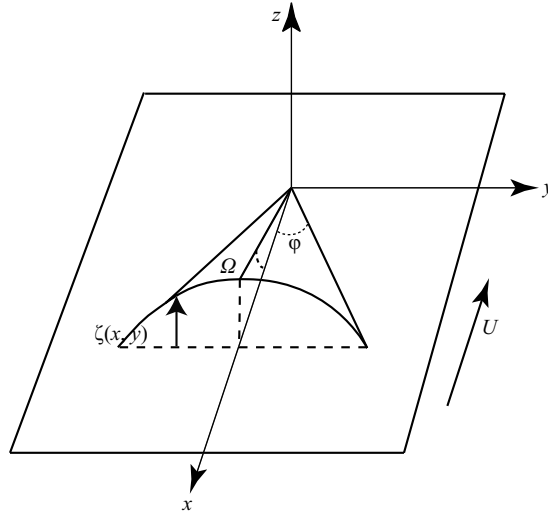


FIGURE 19. Diagram of the rear of a drop on a plate moving upwards at the velocity U such that the drop is in the corner regime. The tail is assumed to be a corner with the opening half-angles φ and Ω . ζ represents the height of the the drop for a given x and y .

We would like to thank Howard Stone for comments and a critical reading of the manuscript. We are also indebted to Bruno Andreotti for advice on this experiment and to Emmanuelle Rio, Jacco Snoeijer and Valery Roy for helpful discussions.

Appendix. A simple way to link the in-plane and out-of-plane angles of the cone

Let (x, y, z) be the axes defined on figure 19. The tail of the drop can be approximated to a parabola, an assumption supported by the views from the side of the drops. Therefore the height ζ of the drop can be related to x and y by

$$\zeta(x, y) \simeq \Omega x \left(1 - \frac{y^2}{x^2 \tan^2 \varphi} \right). \quad (\text{A } 1)$$

A relationship between the angles φ and Ω is given by a lubrication constraint. The balance of downwards and upwards liquid flow in the framework of the drop gives the following equation:

$$U \zeta \simeq - \frac{h^3}{3\eta} \frac{\partial P}{\partial x} \quad (\text{A } 2)$$

where the pressure P is close to $\gamma h_{yy} = 2\gamma\Omega/(x \tan^2 \varphi)$. Hence we obtain

$$\Omega^3 = \frac{3}{2} Ca \tan^2 \varphi \quad (\text{A } 3)$$

which is the same as equation (5.8), since $\tan \Omega \simeq \Omega$.

REFERENCES

- BEN AMAR, M., CUMMINGS, L. & POMEAU, Y. 2001 Singular points on a receding contact line. *C. R. Acad. Sci. Paris* **329**, II-b, 277–282.
- BEN AMAR, M., CUMMINGS, L. J. & POMEAU, Y. 2003 Transition of a moving contact line from smooth to angular, *Phys. Fluids* **15**, 2949–2960.
- BIKERMAN, J. J. 1950 Sliding of drops from surfaces of different roughness, *J. Colloid Sci.* **5**, 349–359.
- BLAKE, T. D. & RUSCHAK, K. J. 1979 A maximal speed of wetting, *Nature* **282**, 489–491.

- BLAKE, T. D. & RUSCHAK, K. J. 1997 Wetting: static and dynamic contact lines. In *Liquid Film Coating—Scientific Principles and their Applications* (ed. S. F. Kistler & P. M. Schweizer), pp. 63–97. Chapman & Hall.
- COHEN, I. & NAGEL, S. R. 2002 Scaling at a selective withdrawal transition through a tube suspended above the fluid surface. *Phys. Rev. Lett.* **88**, 074501.
- COX, R. G. 1986 The dynamics of the spreading of liquids on a solid surface. *J. Fluid. Mech.* **168**, 169–194.
- DAERR, A., LE GRAND, N., LIMAT, L. & STONE, H. A. 2003 Drops sliding along an inclined plane: Experiments versus 3D hydrodynamic model. *Proc. 5th European Coating Symposium, Friburg* (ed. P. M. Schweizer).
- DERJAGUIN, B. V. & LEVI, S. M. 1964 *Film Coating Theory*. Focal Press, London.
- DUSSAN, V., E. B. 1979 On the spreading of liquids on solid surfaces: static and dynamic contact lines. *Annu. Rev. Fluid Mech.* **11**, 371–400.
- DUSSAN, V., E. B. 1985 On the ability of drops or bubbles to stick to non-horizontal surfaces of solids, Part 2: small drops or bubbles having contact angles of arbitrary size. *J. Fluid Mech.* **151**, 1–20.
- DUSSAN, V., E. B. & CHOW, R. T.-P. 1983 On the ability of drops or bubbles to stick to non-horizontal surfaces of solids. *J. Fluid Mech.* **137**, 1–29.
- EGGERS, J. 2004 Toward a description of contact line motion at higher capillary numbers. *Phys. Fluids* **16**, 3491–3494.
- EGGERS, J. 2005 Instability of a moving contact line. *J. Fluid. Mech.* (submitted).
- FURMIDGE, C. G. L. 1962 Studies at phase interfaces, I. The sliding of liquid drops on solid surfaces and a theory for spray retention. *J. Colloid Sci.* **17**, 309–324.
- DE GENNES, P.-G. 1986 Deposition of Langmuir-Blodgett layers. *Colloid Polymer Sci.* **264**, 463–465.
- DE GENNES, P.-G., HUA, X. & LEVINSON, P. 1990 Dynamics of wetting: local contact angles. *J. Fluid Mech.* **212**, 55–63.
- GOLESTANIAN, R. & RAPHAEL, E. 2001 Relaxation of a moving contact line and the Landau-Levich effect. *Eurphys. Lett.* **55**, 228–234.
- GOLESTANIAN, R. & RAPHAEL, E. 2003 Roughening transition in a moving contact line. *Phys. Rev. E* **67**, 031603.
- KIM, H.-Y., LEE, H.-J. & KANG, B.-H. 2002 Sliding of liquid drops down an inclined solid surface. *J. Colloid Sci.* **247**, 372–380.
- KISTLER, S. F. & SCHWEIZER, P. M. (Eds.) 1997 *Liquid Film Coating – Scientific Principles and their Technological Implications*. Chapman & Hall.
- LIMAT, L., PODGORSKI, T., FLESSELLES, J.-M., FERMIGIER, M., MOAL, S., STONE, H. A., WILSON, S. K. & ANDREOTTI, B. 2001 Shape of drops sliding down an inclined surface. *Proc. 4th European Coating Symposium, Bruxelles* (ed. J.-M. Buchlin & J. Anthoine).
- LIMAT, L. & STONE, H. A. 2004 Three-dimensional lubrication model of a contact line corner singularity. *Eurphys. Lett.* **65**, 365–371.
- PODGORSKI, T. 2000 Ruissellement en conditions de mouillage partiel. PhD thesis, Paris 6 University, Paris, France.
- PODGORSKI, T., FLESSELLES, J.-M. & LIMAT, L. 2001 Corners, cusps and pearls in running drops. *Phys. Rev. Lett.* **87**, 036102–036105.
- POMEAU, Y. 2000 Représentation de la ligne de contact mobile dans les équations de la mécanique des fluides. *C. R. Acad. Sci. Paris* **328**, II-b, 411–416.
- POMEAU, Y. 2002 Recent progress in the moving contact line problem: a review. *C. R. Méc.* **330**, 207–222.
- RIO, E., DAERR, A., ANDREOTTI, B. & LIMAT, L. 2005 Boundary conditions in the vicinity of a dynamic contact line: Experimental investigation of viscous drops sliding down an inclined plane. *Phys. Rev. Lett.* **94**, 024503.
- RUIJTERS, M. J., BLAKE, T. D. & DE CONINCK, J. 1999 Dynamic wetting studied by molecular modeling simulations of droplet spreading. *Langmuir* **15**, 7836–7847.
- STONE, H. A., LIMAT, L., WILSON, S. K., FLESSELLES, J.-M. & PODGORSKI, T. 2001 Corner singularity of a contact line moving on a solid surface. *C. R. Physique* **3**, 103–110.
- VOINOV, O. V. 1976 Hydrodynamics of wetting. *Fluid Dyn.* **11**, 714–721.